RESEARCH ARTICLE

ADVANCED OPTICAL MATERIALS
www.advopticalmat.de

Multiscale Physics-Informed Neural Networks for the Inverse Design of Hyperuniform Optical Materials

*Roberto Riganti, Yilin Zhu, Wei Cai, Salvatore Torquato, and Luca Dal Negro**

In this study, multiscale physics-informed neural networks (MscalePINNs) are employed for the inverse design of finite-size photonic materials with stealthy hyperuniform (SHU) disordered geometries. Specifically, MscalePINNs are shown to capture the fast spatial variations of complex fields scattered by arrays of dielectric nanocylinders arranged according to isotropic SHU point patterns, thus enabling a systematic methodology to inversely retrieve their effective dielectric profiles. This approach extends the recently developed high-frequency homogenization theory of hyperuniform media and retrieves more general permittivity profiles for applications-relevant finite-size SHU and optical systems, unveiling unique features related to their isotropic nature. In particular, the existence of a transparency region beyond the long-wavelength approximation is numerically corroborated, enabling the retrieval of effective and isotropic locally homogeneous media even without disorder-averaging, in contrast to the case of uncorrelated Poisson random patterns. The flexible multiscale network approach introduced here enables the efficient inverse design of more general effective media and finite-size optical metamaterials with isotropic electromagnetic responses beyond the limitations of traditional homogenization theories.

1. Introduction

Disordered hyperuniform systems were recently discovered in a variety of contexts and phenomena, including glass formation, spin systems, photonic band structures and radiation engineering, nanophotonics, and biological systems, to name a few.[1,2] A hyperuniform point pattern is characterized by the vanishing of its structure factor $S(\boldsymbol{k})$ when the wavevector goes to zero, resulting in the suppression of long-wavelength density fluctuations.[3,4] In the context of condensed matter physics, it was shown that two- and three-dimensional systems of particles can freeze into highly degenerate disordered hyperuniform states at zero temperature with stealthy hyperuniform (SHU) point pattern geometry, challenging the traditional belief that liquids freeze into highly symmetric structures.[5–7] Among the hyperuniform states of matter, SHU systems are characterized by a structure factor that vanishes over a compact interval of wavevectors. Therefore, stealthy hyperuniformity is a stronger condition than standard hyperuniformity because single scattering events are prohibited within a large interval of spatial frequencies, thus suppressing the corresponding far-field radiation over sizeable angular ranges. Importantly, the structural correlation properties of disordered SHU media can be largely controlled by the χ stealthiness parameter, which equals the ratio of the number of constrained wave vectors in reciprocal space to the total number of degrees of freedom, providing opportunities for tuning the structures in between traditional (uncorrelated) random media for $\chi = 0\%$ and highly correlated (periodic) structures for $\chi = 100\%$. Moreover, it was established that the degree of short-range order in these systems increases with χ, inducing a transition from disordered to crystalline phases when $\chi > 50\%$ in two spatial dimensions. Recently, the interaction of hyperuniform media with electromagnetic waves attracted significant interest resulting in the discovery of amorphous materials with large and complete photonic bandgaps, photon sub-diffusion and localization, as well as in the engineering of enhanced light absorbers, quantum cascade lasers, directional extractors of incoherent emission for light-emitting diodes, free-form waveguides, and Luneburg lenses.[6,8–15] Moreover, the effective electromagnetic wave properties of stealthy hyperuniform systems have been studied beyond the quasistatic regime within a rigorously valid nonlocal theory in the thermodynamic limit of infinite system size, leading to the prediction of perfect transparency intervals up to finite wavenumbers.[16–19] This characteristic

R. Riganti, L. D. Negro
Department of Physics
Boston University
590 Commonwealth Avenue, Boston, MA 02215, USA
E-mail: dalnegro@bu.edu
Y. Zhu, L. D. Negro
Division of Material Science and Engineering
Boston University
15 Saint Mary's Street, Brookline, MA 02446, USA
W. Cai
Department of Mathematics
Southern Methodist University
3200 Dyer Street, 208 Clements Hall, Dallas, TX 75275, USA
S. Torquato
Department of Chemistry and Physics, and Princeton Materials Institute
Princeton University
Frick Laboratory, 160, Princeton, NJ 08544, USA
L. D. Negro
Department of Electrical and Computer Engineering and Photonics Center
Boston University
8 Saint Mary's Street, Boston, MA 02215, USA

DOI: 10.1002/adom.202403304

"transparency regime" is manifested by a vanishing imaginary part of the effective dielectric constant ϵ_e of the scattering structure within a prescribed range of wavelengths.[16,17] Recent work has shown that this transparency is robust against multiple scattering, opening the doors to numerous improvements in the design of photonic materials with applications ranging from light harvesting in solar cells[20] to the design of waveguides.[21–25] However, dynamic homogenization theory cannot be directly applied to finite-size structures when the strength of the multiple scattering renders the effective permittivity spatially dependent. This limitation establishes the need for a more general predictive approach intended for the inverse design of the effective wave characteristics of disordered hyperuniform media and photonic devices.[26–28]

In this study, we propose and develop an accurate and flexible deep-learning methodology to design novel optical materials by predicting the effective electromagnetic properties of finite-size hyperuniform structures in the dynamic scattering regime based on multiscale physics-informed neural networks (MscalePINNs). Specifically, we apply this approach to disordered SHU and Poisson arrays of dielectric nanopillars of radius a with constant relative permittivity ϵ_r and demonstrate enhanced transparency enabling the accurate inverse retrieval of the effective dielectric permittivity $\hat{\varepsilon}(x, y; k)$ of SHU structures with different sizes, shapes, and dielectric contrast values. Our results for SHU structures show accurate inverse retrieval of dielectric properties without averaging over multiple disorder realizations, in contrast to the case of the uncorrelated Poisson patterns of equivalent density. Moreover, we show that SHU arrays allow for the retrieval of a locally homogeneous medium at shorter wavelengths compared to Poisson arrays with identical particle volume fractions, conjecturing that SHU structures are transparent over a wider range of wavelengths even in finite-size systems. Importantly, we also establish through numerous examples that MscalePINN is a necessary extension of traditional single-scale PINN platforms in situations where significant multiple scattering effects contribute to determine the effective parameters. Furthermore, by exciting with plane waves at different angles, we show that finite-size SHU arrays feature an isotropic locally homogeneous response, i.e., the retrieved effective parameters do not depend on the angle of the incoming radiation. Finally, we introduce an improved architecture of MscalePINN for retrieving binary effective optical media that are suitable for experimental demonstration using available nanofabrication techniques. In order to present a comprehensive analysis, we vary the size, shape, incident wavelength, number of scatterers, stealthiness parameter, and direction of excitation for the investigated structures. Our accompanying Supporting Information details all the relevant calculation parameters and provides additional comparisons with single-scale PINN calculations.

2. Experimental Section

In optical science and photonics technology, it is often required to solve differential or integro-differential models governing the scattering and transport of vector waves inside complex and heterogeneous materials or in extended media containing resonant optical nanostructures.[29–31] While many advanced techniques have been developed for the forward solution of such mathematical problems, the multiscale structure of heterogeneous media generally prevents the accurate and efficient solution of inverse scattering problems of relevance to imaging, acoustics, geophysics, remote sensing, and nondestructive testing. Specifically, in the regime of multiple wave scattering where the transport mean free path ξ_t is smaller than the system's size L, the inversion of differential models becomes a nonlinear and computationally intractable problem for traditional numerical techniques. This prevents the accurate prediction of the desired parameters of multi-particle complex structures from a limited set of available field data, driving the development of alternative and more powerful computational frameworks that leverage automatic learning techniques and optimization methods.[32–36] Specifically, in the context of photonic inverse design, machine learning and deep learning techniques have been employed for the design of state-of-the-art metasurfaces, nanodevices, and more.[34,37–51]

Motivated by the versatility and predictive power of these techniques, recent developments in scientific machine learning (ML) introduced physics-informed neural networks (PINNs) as a viable approach to solve forward and inverse integro-differential problems efficiently and with minimal computational overhead.[52–55] Unlike standard deep learning approaches, PINNs restrict the space of admissible solutions by enforcing the validity of the PDE models governing the actual physics of the problem. This is achieved by using relatively simple feed-forward neural network architectures as trainable surrogate solutions of the partial differential equations (PDEs) on the interior and boundary points of their definition domains and leveraging automatic differentiation (AD) techniques readily available in all the most powerful machine learning packages.[52–54,56] Specifically, PINNs are trained on a set of randomly distributed collocation points to minimize the PDE residues in a suitable norm.[53,54] Therefore, PINNs can use as little as one training dataset to obtain the desired inverse solutions, thus relaxing the burdens often imposed by the massive datasets utilized by alternative, i.e., non-physics-constrained, traditional data-driven deep learning approaches.[33] These characteristics render PINNs uniquely effective in solving differential and integro-differential inverse problems with a minimal overhead compared to the corresponding forward problem.[55,57–59]

2.1. Mathematical Formulation of MscalePINN

Recently, it became apparent in the ML community that deep neural networks (DNNs) learn the low-frequency content of available training data quickly and with a good generalization error but fail to do so when high-frequency data are involved. This general Fourier-type principle creates an implicit spectral bias as DNNs preferentially fit training data using low-frequency functions.[50,60–63] To solve this issue in the context of PINNs simulations, the approach of multiscale PINN (MscalePINN) was recently introduced. MscalePINN employs different sub-networks specialized to learn down-shifted frequency representations of the original datasets and functions by converting the learning and approximation of high-frequency data to that of low-frequency ones.[64,65]

To illustrate the approach of the multiscale PINN, a band-limited function $f(\mathbf{x})$, $\mathbf{x} \in \mathbb{R}^d$ was considered, whose Fourier transform $\hat{f}(\mathbf{k})$ has a compact support, i.e.,

$$\mathrm{Supp}\hat{f}(\mathbf{k}) \subset B(K_{\max}) = \{\mathbf{k} \in \mathbb{R}^d, |\mathbf{k}| \leq K_{\max}\} \tag{1}$$

The domain $B(K_{\max})$ can be patitioned as a union of M concentric annulus with uniform or non-uniform width, e.g., for the case of uniform width K_0,

$$A_i = \{\mathbf{k} \in \mathbb{R}^d, (i-1)K_0 \leq |\mathbf{k}| \leq iK_0\},$$
$$K_0 = K_{\max}/M, \quad 1 \leq i \leq M \tag{2}$$

so that

$$B(K_{\max}) = \bigcup_{i=1}^{M} A_i \tag{3}$$

As a result, the function $\hat{f}(\mathbf{k})$ can be decomposed in the Fourier domain as before

$$\hat{f}(\mathbf{k}) = \sum_{i=1}^{M} \chi_{A_i}(\mathbf{k})\hat{f}(\mathbf{k}) \triangleq \sum_{i=1}^{M} \hat{f}_i(\mathbf{k}) \tag{4}$$

and

$$\mathrm{Supp}\hat{f}_i(\mathbf{k}) \subset A_i \tag{5}$$

This decomposition in the Fourier space gives a corresponding one in the physical space

$$f(\mathbf{x}) = \sum_{i=1}^{M} f_i(\mathbf{x}) \tag{6}$$

where

$$f_i(\mathbf{x}) = \mathcal{F}^{-1}[\hat{f}_i(\mathbf{k})](\mathbf{x}) \tag{7}$$

From Equation (5), a simple downward scaling can be applied to convert the high frequency region A_i to a low-frequency one. Namely, a scaled version of $\hat{f}_i(\mathbf{k})$ is defined as

$$\hat{f}_i^{(\mathrm{scale})}(\mathbf{k}) = \hat{f}_i(\alpha_i \mathbf{k}), \qquad \alpha_i > 1 \tag{8}$$

and, correspondingly, in the physical space

$$f_i^{(\mathrm{scale})}(\mathbf{x}) = \frac{1}{\alpha_i^d} f_i\left(\frac{1}{\alpha_i}\mathbf{x}\right) \tag{9}$$

or

$$f_i(\mathbf{x}) = \alpha_i^d f_i^{(\mathrm{scale})}(\alpha_i \mathbf{x}) \tag{10}$$

So, the spectrum of the scaled function $\hat{f}_i^{(\mathrm{scale})}(\mathbf{k})$ is of low frequency if α_i is chosen large enough, i.e.,

$$\mathrm{Supp}\hat{f}_i^{(\mathrm{scale})}(\mathbf{k}) \subset \{\mathbf{k} \in \mathbb{R}^d, \frac{(i-1)K_0}{\alpha_i} \leq |\mathbf{k}| \leq \frac{iK_0}{\alpha_i}\} \tag{11}$$

Now with DNN's preference toward low-frequency learning, with iK_0/α_i being small, i.e. $iK_0/\alpha_i = O(2\pi/L)$, where L is the characteristic length of the cluster, we can train a DNN $f_{\theta^{n_i}}(\mathbf{x})$ to learn $f_i^{(\mathrm{scale})}(\mathbf{x})$ quickly

$$f_i^{(\mathrm{scale})}(\mathbf{x}) \sim f_{\theta^{n_i}}(\mathbf{x}) \tag{12}$$

giving an approximation to $f_i(\mathbf{x})$ immediately

$$f_i(\mathbf{x}) \sim \alpha_i^d f_{\theta^{n_i}}(\alpha_i \mathbf{x}) \tag{13}$$

and, to $f(\mathbf{x})$ as well

$$f(\mathbf{x}) \sim \sum_{i=1}^{M} \alpha_i^d f_{\theta^{n_i}}(\alpha_i \mathbf{x}) \tag{14}$$

giving the format of the MscalePINN.[64,65] The scale factors α_i can also be converted into trainable parameters to best fit the target functions. In fact, the factor α_i^d can be absorbed into the weights of the last layer, being linear in most cases, of the sub-network $f_{\theta^{n_i}}(\alpha_i \mathbf{x})$. Therefore, the factor α_i^d outside the sub-network can be set to be one to avoid involving large values when α_i or d is large without affecting the overall efficiency of MscalePINN after training. Each sub-network with scaled inputs can be written as:

$$f_\theta(x) = W^{[L-1]}\sigma\circ(\dots(W^{[1]}\sigma\circ(W^{[0]}x + b^{[0]}) + b^{[1]})\dots) + b^{[L-1]} \tag{15}$$

The general MscalePINN architecture employed in this study is shown in **Figure 1a**. The unscaled spatial input parameters x, y were passed through n independent sub-networks $u_i(\alpha_i x, \alpha_i y; \tilde{\boldsymbol{\theta}}_i)$ with activation function $\sin(\boldsymbol{x})$, scaling α_i, and hyperparameters $\tilde{\boldsymbol{\theta}}_i$. The output of each sub-network u_i was then combined into the MscalePINN solution $\hat{u}(x, y; \tilde{\boldsymbol{\theta}})$ according to Equation (14) and then, through automatic differentiation, it was used to satisfy the PDE, boundary and initial conditions of the differential equation. The improvement in the expressive power of the MscalePINN architecture compared to traditional PINNs was due to the enhanced convergence across a wide range of frequencies through the scaling of the input $\boldsymbol{x}$ with a factor α_i together with the sinusoidal activation function $\sin(\boldsymbol{x})$. In the diagram shown in Figure 1b,a schematic illustrating the basic idea behind the MscalePINN approach is presented. In this diagram, a representative short-wavelength training field is displayed, where each component of the electric field is composed of multiple spatial frequencies. To tackle this multiscale problem, each MscalePINN sub-network solved the Helmholtz equation in a "zoomed-in" sub-domain defined by $\alpha_i \cdot \boldsymbol{X}$. That is, the product of α_i and the unnormalized spatial inputs allowed the sine activation function MscalePINN to access different spatial frequency information in each sub-network. In doing so, the MscalePINN architecture can precisely tackle the forward and inverse multiscale solutions of complex electromagnetic problems. For this reason, the convergence and accuracy of the method for inverse problems can be improved by extracting spectral information from the inverse training datasets to inform the settings of the multiscale sub-networks.

For inverse electromagnetic problems, the following PDE was considered with the unknown permittivity distribution $\epsilon(x, y; k)$,

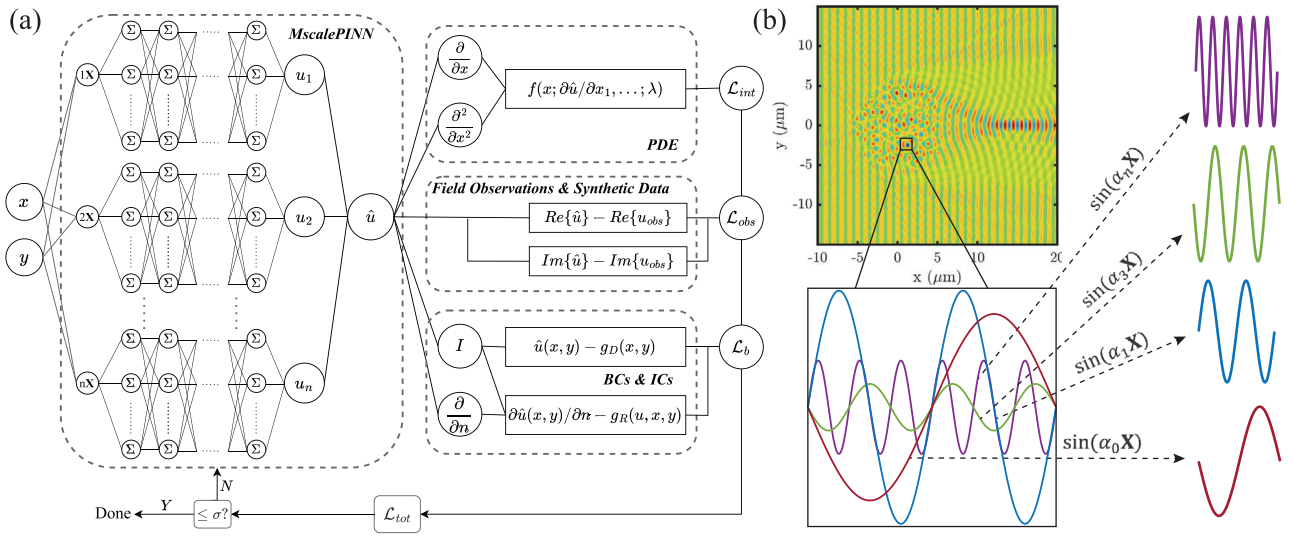

Figure 1. a) Schematics of the MscalePINN architecture employed for the inverse design of photonic structures. b) Diagram displaying MscalePINN's training approach in practice. In regions of the electromagnetic field with large frequency components, MscalePINN's sub-networks can train on a specialized sub-domain of interest and avoid the spectral bias.

generally wavevector-dependent, for the surrogate solution $\hat{u}(\boldsymbol{x})$ with $\boldsymbol{x} = (x_1, \ldots, x_d)$ defined on a domain $\Omega \subset \mathbb{R}^d$:[55,57]

$$\varphi\left(\boldsymbol{x}; \hat{u}, \frac{\partial \hat{u}}{\partial x_1}, \ldots, \frac{\partial \hat{u}}{\partial x_d}; \frac{\partial^2 \hat{u}}{\partial x_1^2}, \ldots, \frac{\partial^2 \hat{u}}{\partial x_1 \partial x_d}; \ldots; \varepsilon\right) = 0 \tag{16}$$

The calculated values were then combined into the global loss function $\mathcal{L}(\tilde{\theta})$, generally of the form:

$$\mathcal{L}(\tilde{\theta}) = \mathcal{L}_{int}(\tilde{\theta}; \mathcal{N}_{int}) + \mathcal{L}_b(\tilde{\theta}; \mathcal{N}_b) + \mathcal{L}_{inv}(\tilde{\theta}; \mathcal{N}_{inv}) \tag{17}$$

In the loss function above, the component

$$\mathcal{L}_{int}(\tilde{\theta}; \mathcal{N}_{int}) = \frac{1}{|\mathcal{N}_{int}|} \sum_{(x,y)\in\mathcal{N}_{int}} \left|\left|\varphi\left(x, y; \hat{u}, \frac{\partial \hat{u}}{\partial x}, \frac{\partial \hat{u}}{\partial y}, \ldots, \frac{\partial^2 \hat{u}}{\partial y^2}; \varepsilon_r\right)\right|\right|_2^2 \tag{18}$$

represents the loss term calculated for the PDE in the interior of the domain Ω and

$$\mathcal{L}_b(\tilde{\theta}; \mathcal{N}_b) = \frac{1}{|\mathcal{N}_b|} \sum_{(x,y)\in\mathcal{N}_b} ||\mathcal{B}(\hat{u}, x, y)||_2^2 \tag{19}$$

is the loss term for the boundary conditions of the PDE, where $(x, y) \in \partial\Omega$. Finally, in order to solve general inverse electromagnetic problems,

$$\mathcal{L}_{inv}(\tilde{\theta}; \mathcal{N}_{inv}) = \frac{1}{|\mathcal{N}_{inv}|} \sum_{(x,y)\in\mathcal{N}_{inv}} ||\mathrm{Re}[\hat{u}(x, y)] - \mathrm{Re}[u_{obs}(x, y)]||_2^2 + ||\mathrm{Im}[\hat{u}(x, y)] - \mathrm{Im}[u_{obs}(x, y)]||_2^2 \tag{20}$$

is introduced as the inverse loss term calculated on the real and imaginary parts of a complex field obtained through numerical simulations, and $\mathcal{N}_{int}$, $\mathcal{N}_b$, $\mathcal{N}_{inv}$ are the number of residual points for each loss term. In the next section, the specific implementation of MscalePINN employed in this work is described.

2.2. MscalePINN for Electromagnetic Design

This study deals with electromagnetic parameter retrieval and homogenization problems for which the Helmholtz equation was used to constrain MscalePINNs and retrieve the effective model parameters of optical materials. In particular, the complex Helmholtz equation was considered for inhomogeneous two-dimensional effective media under TM polarization excitation:

$$\nabla^2 E_z(x, y) + \epsilon_r(x, y; k) k_0^2 E_z = 0 \tag{21}$$

where E_z is the z-component of the electric field, $k_0 = \frac{2\pi}{\lambda}$ is the wavenumber in free space, and $\epsilon_r(x, y; k)$ is the relative permittivity of the inhomogeneous effective medium (spatially dependent), which is almost constant in the case of a homogenized effective medium at sufficiently long wavelengths. Because E_z and $\epsilon_r(x, y; k)$ are complex variables, separating Equation (21) into real and imaginary parts yields:

$$\begin{aligned} \nabla^2 \mathrm{Re}[E_z](x, y) &= -\mathrm{Re}[E_z]\mathrm{Re}[\epsilon_r(x, y; k)]k_0^2 + \mathrm{Im}[E_z]\mathrm{Im}[\epsilon_r(x, y; k)]k_0^2 \\ \nabla^2 \mathrm{Im}[E_z](x, y) &= -\mathrm{Im}[E_z]\mathrm{Re}[\epsilon_r(x, y; k)]k_0^2 - \mathrm{Re}[E_z]\mathrm{Im}[\epsilon_r(x, y; k)]k_0^2 \end{aligned} \tag{22}$$

This framework enables to predict $\mathrm{Re}[\epsilon_r(x, y; k)]$ and $\mathrm{Im}[\epsilon_r(x, y; k)]$ independently for the inhomogeneous effective medium and therefore to naturally quantify the radiation losses that are particularly difficult to account within the effective index theory.[66,67]

Using the introduced MscalePINNs framework, the effective permittivity parameter $\epsilon_r(x, y; k)$ of the Helmholtz equation was inversely retrieved by training the MscalePINNs over a spatial grid of collocation points and a synthetic dataset composed of complex field values generated by solving the forward scattering problem using COMSOL Multiphysics.[68] For each SHU or Poisson array considered, the full complex field in COMSOL was first generated and then exported the real and imaginary parts in grids

of a maximum of 350 × 350 points. Smaller grids of 100 × 100 points were sufficient to sample long-wavelength fields, but for short-wavelength fields, we needed to increase the sampling rate. The general electromagnetic loss function in Equation (17) was therefore adapted to the problem by introducing two $\mathcal{L}_{int}(\tilde{\theta};\mathcal{N}_{int})$ terms, one for the real and one for the imaginary part of Equation (21). Similarly, the inverse loss term $\mathcal{L}_{inv}(\tilde{\theta};\mathcal{N}_{inv})$ was split into two terms, one for the real and one for the imaginary part of the field E_z. For this inversion problem, it was not needed to include a boundary condition loss term $\mathcal{L}_b(\tilde{\theta};\mathcal{N}_b)$. The final MscalePINN loss function is:

$$\mathcal{L}(\tilde{\theta}) = \mathcal{L}_{\mathrm{Re},int}(\tilde{\theta};\mathcal{N}_{\mathrm{Re},int}) + \mathcal{L}_{\mathrm{Im},int}(\tilde{\theta};\mathcal{N}_{\mathrm{Im},int}) + \mathcal{L}_{\mathrm{Re},inv}(\tilde{\theta};\mathcal{N}_{\mathrm{Re},inv}) + \mathcal{L}_{\mathrm{Im},inv}(\tilde{\theta};\mathcal{N}_{\mathrm{Im},inv}) \quad (23)$$

After each training was completed and the total loss decreases to a minimum of 10^{-2}, the precision of the effective medium retrieved following the methodology that was introduced in references was evaluated.[55,57] To establish the accuracy of the results, a forward FEM simulation was performed in COMSOL using the retrieved $\hat{\varepsilon}(x,y;k)$, and real and imaginary parts of the fields were compared with those resulting from considering the actual geometry of the arrays. Moreover, in this work, the resulting accuracy was quantified using the relative L_1 error defined in the Supporting Information S4. If the relative L_1 error against the original FEM field was low enough (⩽10%), then MscalePINN retrieved an accurate effective medium. However, for the loss functions, MscalePINN was trained with L^2 functions (also known as mean squared error functions[54]) that emphasized large errors nonlinearly, a feature required to retrieve structures in the multiple scattering regime with high accuracy. Furthermore, as additional post-processing, for each retrieved $\hat{\varepsilon}(x,y;k)$, the average and standard deviation of its real and imaginary components were calculated inside an area with a radius equal to the size of the array. The average over the imaginary part ($\langle \mathrm{Im}[\hat{\varepsilon}(x,y;k)]\rangle$) will determine the onset of the transparency regime predicted by Torquato et al.[16,17] In contrast, the average and standard deviation over the real part ($\langle \mathrm{Re}[\hat{\varepsilon}(x,y;k)]\rangle$, $\sigma\{\langle \mathrm{Re}[\hat{\varepsilon}(x,y;k)]\rangle\}$) will characterize the degree of spatial homogeneity of the retrieved effective medium while providing a quantitative metric to compare with results from traditional effective medium theory, such as the Bruggeman mixing formula.[66] It will be shown that, in the long wavelength regime, the average over the real part of $\hat{\varepsilon}(x,y;k)$ will agree with the predictions based on the Bruggeman formula. However, it is shown that the method can also be successfully utilized at shorter wavelengths and in finite-size device structures of arbitrary shapes beyond the reach of traditional homogenization theories. Throughout this study, different MscalePINN architectures are employed and, for this reason, Table S1 (Supporting Information) is included that lists all the relevant hyperparameters employed in our study for each architecture. In addition, Table S1 (Supporting Information) lists the size of the synthetic dataset of collocation points employed during training. All the codes were developed in-house using TensorFlow,[69] and numerical simulations were performed using different GPUs depending on the problem, i.e., either an NVIDIA P100, NVIDIA V100, or NVIDIA A40 was employed.

3. Results and Discussion

3.1. MscalePINN Versus Single-Scale PINN Beyond the Long-Wavelength Regime

We begin our study by showing in **Figure** 2a direct comparison between the retrieved effective medium profiles obtained using the multiscale and the traditional single-scale PINN for a stealthy hyperuniform array with $N = 663$ dielectric nanocylinders of radius $a = 67.5$ nm, packing fraction $\phi = 0.16$, and array diameter $L \approx 8.5$ μm. Here $\phi = \rho v(a)$, where ρ is the number density of the array and $v(a)$ is the cross-sectional area of the nanocylinders. We have included the point pattern employed for this comparison in Figure S2 (Supporting Information). For this comparison, we have selected three different datasets for performing the training for the inverse permittivity retrieval. These datasets are the distributions of the complex total fields by the SHU structure at different wavelengths with respect to the predicted "transparency regime" according to the inequality below that characterizes the full extent of the transparency region:[17]

$$k_0\rho^{-1/2} = 2\pi\frac{\langle d\rangle}{\lambda} \lesssim 1.5, \quad \rho = \frac{N}{\pi R^2} \quad (24)$$

where R is the radius of the SHU array. For the SHU structure considered in this example, the inequality (24) can be satisfied up to the threshold wavenumber $k_{th} \approx 5.4$ μm^{-1}. Figure 2a, b show the agreement of the multi-scale and single-scale PINNs for an incident $k_0 = 2.0$ μm^{-1} (corresponding to $\lambda = 3.14$ μm). This agreement is expected since this k_0 value is well below the threshold value for the transparency region. In Figure 2c,d, however, we notice that the single-scale PINN architecture cannot properly retrieve an effective medium for $k_0 = 4.0$ μm^{-1} ($\lambda = 1.57$ μm) since this wavenumber value is much closer to the edge of the transparency region. In contrast, the MscalePINN has no trouble retrieving a well-localized and homogeneous effective medium even at $k_0 = 4.0$ μm^{-1}. Finally, in panels (e) and (f), we show the complete failure of single-scale PINN to retrieve a physically meaningful effective medium distribution when the wavenumber of the incoming radiation crosses the transparency edge and enters the strong multiple scattering regime at $k_{th} = 5.5$ μm^{-1} ($\lambda = 1.14$). On the other hand, the MscalePINN retrieves a well-localized, albeit inhomogeneous, effective medium also in this case. Therefore, the developed MscalePINN is a powerful extension of the traditional single-scale PINN that becomes necessary when solving the inverse parameter retrieval problem in the multiple scattering regime. Additional characterizations of the investigated SHU structure and the utilized training fields can be found in Figures S2 and S3 of our Supporting Information. Furthermore, we have included a comparison of the training loss functions for the single-scale PINN and MscalePINN employed to generate the structures displayed in **Figure** 4 in the Supporting Information Figure S11. In the next section, we will address the role of disorder averaging in retrieving the effective medium of stealthy hyperuniform and uncorrelated Poisson arrays.

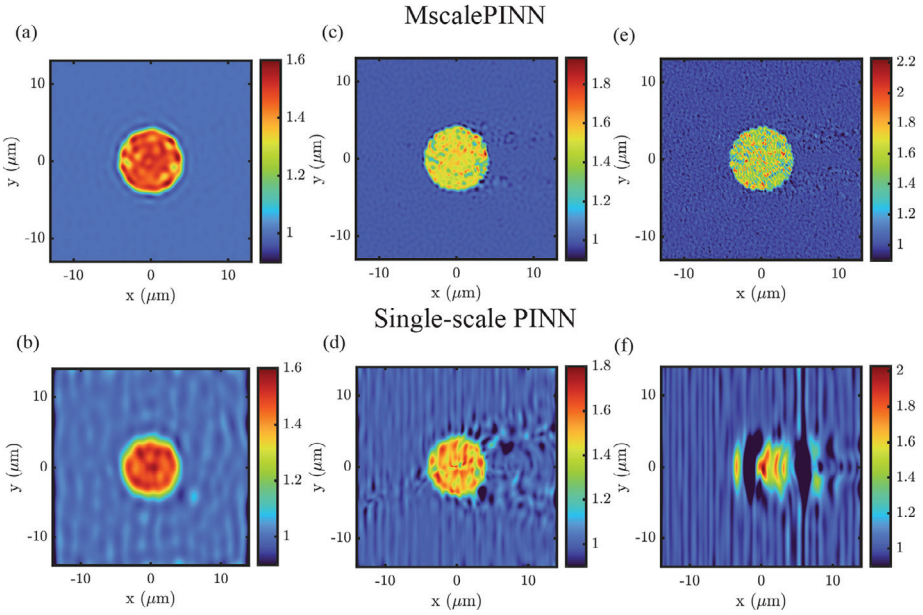

Figure 2. Panels displaying the real part of $\hat{\epsilon}(x, y; k)$. Panels (a), (c), and (e) display the accurately retrieved localized effective medium under incoming field k_0 vector of 2.0, 4.0, and 5.5 μm^{-1} retrieved by MscalePINN. Panels (b), (d), and (f) show that the single-scale PINN can only retrieve an effective medium in the long-wavelength domain, i.e., $k_0 = 2.0\ \mu m^{-1}$, but fails for the higher k_0 vectors 4.0 and 5.5 μm^{-1}.

3.2. MscalePINN Analysis of SHU Ensemble Average

We are interested here in retrieving the homogenized complex permittivity of the SHU array with diameter $L \approx 10$ μm composed of $N = 396$ dielectric nanocylinders of radius $a = 125$nm, displayed in **Figure** 3a. The corresponding structure factor $S(\boldsymbol{k})$ is shown in Figure S1 of the Supporting Information. For this example, we used $\chi = 0.5$, $\epsilon_r = 3.0$, $\langle d \rangle / \lambda = 0.15$, and $\phi = 0.2$, where $\langle d \rangle$ is the average first-neighbor distance of the cylinders in the array. The MscalePINNs utilized to solve this inverse problem is a 4-scale MscalePINNs with 4 layer, each with 64 neurons, and it is trained on the real and imaginary parts of the total electric field considering the excitation wavelength $\lambda = 3.0$ μm.

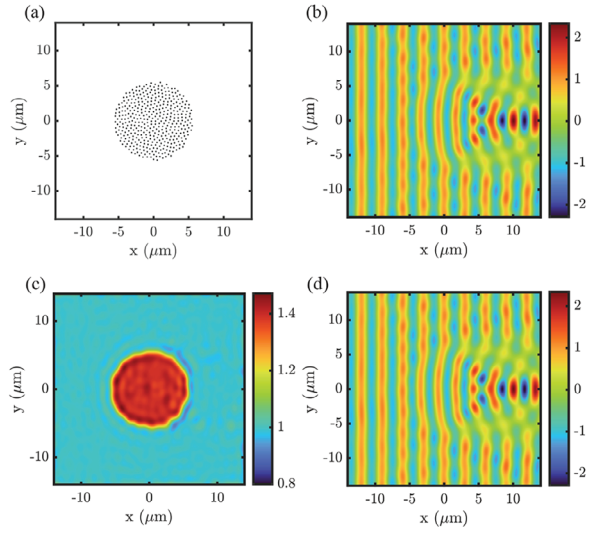

Figure 3. a) SHU array of 396 particles, $\chi = 0.5$, $\epsilon_r = 3.0$, $\langle d \rangle / \lambda = 0.15$ employed for the MscalePINNs homogenization validation. b) The real part of the FEM electric field inverse train dataset is employed to train MscalePINNs to homogenize panel (a). The incident plane wave wavelength is $\lambda = 3.0$ μm. c) MscalePINN's retrieved real part of $\hat{\epsilon}(x, y; k)$, which is then used to perform a forward COMSOL simulation displayed in panel (d) (the real part) to compare with the "true" field used in training.

In Figure 3b, we display the real part of the electric field distribution used during training. The effective permittivity profile $\hat{\epsilon}(x, y; k)$ retrieved by MscalePINNs for a single realization of the investigated SHU array is displayed in panel (c). Remarkably, the effective permittivity is well-localized within the geometrical support of the array with a spatially uniform distribution quantified by the average value $\langle \mathrm{Re}[\hat{\epsilon}(x, y; k)] \rangle = 1.39 \pm 2.8\%$. To better characterize the retrieved homogeneous permittivity profile in the static regime we also calculated the effective medium theory prediction using the Bruggeman mixing formula valid for the bulk case:[66]

$$\sum_i f_i \frac{\epsilon_i - \epsilon_e}{\epsilon_i + \epsilon_e} = 0 \tag{25}$$

where ϵ_e is the effective permittivity, f_i is the filling fraction, and ϵ_i is the permittivity of the i-th component. For a two-phase system under TM polarized incident radiation, Equation 25 reduces to [17]:

$$\epsilon_{brugg} = f_1 \epsilon_1 + f_2 \epsilon_2 \tag{26}$$

For the system studied in Figure 3c it yields $\epsilon_{brugg} = 1.4$, differing only by 0.6% from MscalePINNs and within the uncertainty range predicted. In Figure 3d we display the real part of the total electric field obtained via a forward FEM

Table 1. Comparison of the real part of the homogenized effective permittivity $\hat{\varepsilon}(x, y; k)$ between the ensemble average and single realization for SHU and Poisson structures with the same size.

Structure	Calculation	$\langle \mathrm{Re}[\hat{\varepsilon}(x, y; k)] \rangle$	$\sigma\{\langle \mathrm{Re}[\hat{\varepsilon}(x, y; k)] \rangle$
SHU	Single realization	1.391	2.8%
	Ensemble average	1.404	1.9%
Poisson	Single realization	1.412	8.8%
	Ensemble average	1.413	3.4%

calculation performed using the retrieved permittivity profile from panel (c), which is then used to calculate the L_1 relative error including both the real and imaginary part of the training field. The obtained relative error between the original complex field and the one obtained through the retrieved permittivity parameter was found to be less than 9%, demonstrating the high accuracy of the solution achieved by the developed MscalePINNs.

To further investigate the quality of the reconstruction, we also performed an ensemble average of 10 different SHU configurations all generated with the same stealthiness parameter $\chi = 0.5$, $\epsilon_r = 3.0$, and $N = 395 \pm 5$ and with constant $\phi = 0.2$. Our findings are summarized in the first row of **Table 1**, which displays almost identical results to the single realization case when pointwise spatial averaging is performed over the SHU realizations. As a comparison, we also show in Table 1 the results of the same ensemble averaging procedure performed over 10 different realizations of Poisson uncorrelated random (UR) structures with $\epsilon_r = 3.0$, $N = 395 \pm 5$, and $\phi = 0.2$. We note that, compared to the SHU configuration, the single realization for the Poisson structure features a significant inhomogeneity in the spatial distribution of $\mathrm{Re}[\hat{\varepsilon}(x, y; k)]$ due to the presence of larger fluctuations among the different disorder realizations. However, even in this case the retrieved effective medium permittivity for the Poisson point pattern has a cumulative L^2 training error lower than 10^{-3} and a relative L_1 error lower than 8% when the forward total FEM field of the array was compared to the one obtained from the inversely retrieved permittivity. This indicated that MscalePINNs has retrieved an accurate spatially dependent permittivity, i.e., an inhomogeneous effective medium, demonstrating the importance of the more general network approach developed here. Therefore, we conclude that MscalePINNs retrieved an accurate field distribution and $\hat{\varepsilon}(x, y; k)$ for both the SHU and Poisson arrays and that, at the single realization level, a locally homogeneous permittivity can only be retrieved for the SHU structures. In the next section, we investigate the behavior of the MscalePINN at shorter wavelengths for both the SHU structures and the uncorrelated Poisson arrays, focusing on a scattering regime where $\hat{\varepsilon}(x, y; k)$ cannot be homogenized using conventional mixing formulas.[66]

3.3. SHU and Poisson Point Patterns Beyond the Long Wavelength Regime

To compare the effective medium behavior of SHU and Poisson structures we generate a Poisson array comparable to the SHU structure discussed in Section 3.1 with $N \approx 660$ dielectric nanocylinders of radius $a = 67.5$ nm, $\phi = 0.16$, and diameter $L \approx 8.5$ μm. The arrays and their structure factors $S(\boldsymbol{k})$ are shown in Figure S2 of the Supporting Information. Figure 4a, c show the retrieved $\hat{\varepsilon}(x, y; k)$ through the MscalePINN for $k_0 = 3.0\ \mu\mathrm{m}^{-1}$ and $5.0\ \mu\mathrm{m}^{-1}$, respectively (corresponding to $\lambda = 2.09$ μm and 1.26 μm). The considered SHU structure has $\chi = 0.3$ and $\epsilon_r = 4.0$. We observe that in panels (a) and (c) both solutions are more spatially homogeneous than the corresponding ones shown in panels (b) and (d) for the Poisson pattern. Specifically, for the SHU structure we found $\langle \mathrm{Re}[\hat{\varepsilon}(x, y; k)] \rangle = 1.48 \pm 4\%$ and $\langle \mathrm{Im}[\hat{\varepsilon}(x, y; k)] \rangle = 10^{-3} \approx 0$ for $\lambda = 2.09$ μm and $\langle \mathrm{Re}[\hat{\varepsilon}(x, y; k)] \rangle = 1.51 \pm 6.0\%$ and $\langle \mathrm{Im}[\hat{\varepsilon}(x, y; k)] \rangle = 10^{-3} \approx 0$ for $\lambda = 1.26$ μm. Moreover, we note that for the short-wavelength simulation near the edge of the transparency region (i.e., $k_0 = 5.5\ \mu\mathrm{m}^{-1}$), the MscalePINN retrieves an average value of $\mathrm{Re}[\hat{\varepsilon}(x, y; k)]$ that is different from the Bruggeman predicted value of 1.48.

However, for the retrieved permittivity of the Poisson structures shown in panels (b) and (d), the degree of spatial nonuniformity becomes apparent already away from the SHU critical value of $5.5\ \mu\mathrm{m}^{-1}$. Figure 4b shows the inhomogeneous profile of the real part for the Poisson's effective permittivity profile $\hat{\varepsilon}(x, y; k)$ predicted by the MscalePINNs for $\lambda = 2.09$ μm. For this inhomogeneous effective medium, $\langle \mathrm{Re}[\hat{\varepsilon}(x, y; k)] \rangle = 1.49 \pm 6.8\%$ and $\langle \mathrm{Im}[\hat{\varepsilon}(x, y; k)] \rangle \approx 10^{-3}$, with an L^2 training loss lower than 10^{-3} and a relative L_1 error on the FEM validation of 9%. The inability to retrieve a locally homogeneous effective permittivity is even more apparent at shorter wavelengths (panel d), where for $\lambda = 1.26$ μm the MscalePINN correctly predicts an effective permittivity profile $\hat{\varepsilon}(x, y; k)$ with $\langle \mathrm{Re}[\hat{\varepsilon}(x, y; k)] \rangle = 1.52 \pm 11\%$ shown in Figure 4d, while $\langle \mathrm{Im}[\hat{\varepsilon}(x, y; k)] \rangle \approx 10^{-2}$. This evident failure to

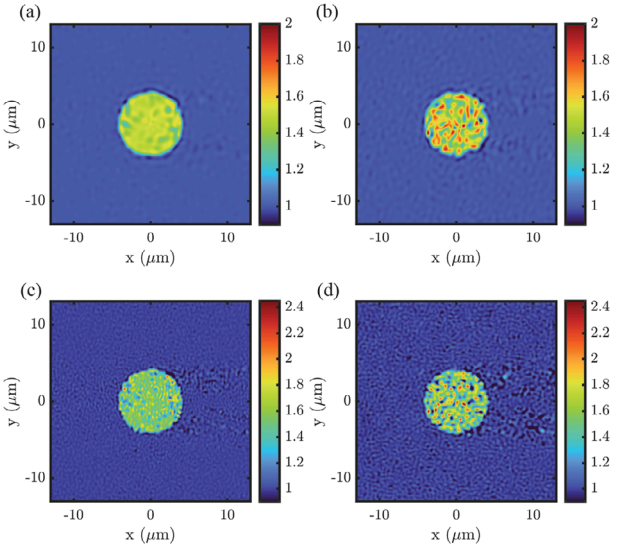

Figure 4. Panels displaying the real part of $\hat{\varepsilon}(x, y; k)$. a) and b) Comparison between the retrieved permittivity profile $\mathrm{Re}[\hat{\varepsilon}(x, y; k)]$ of a stealthy hyperuniform array with $\chi = 0.3$, $N = 663$ particles and the inhomogeneous effective medium of a Poisson array of $N = 661$ particles. The inverse total field used in training had $\lambda = 2.09$ μm ($\langle d \rangle / \lambda = 0.1$), or $k_0 = 3.0\ \mu\mathrm{m}^{-1}$. c) and d) Comparison of the same structures used in panels (a) and (b) but with a lower wavelength of the incident scattering field, $\lambda = 1.26$ μm ($\langle d \rangle / \lambda = 0.14$), or $k_0 = 5.0\ \mu\mathrm{m}^{-1}$. Already at $\lambda = 2.09$ μm, the Poisson array displays evident losses and a more inhomogeneous retrieved $\mathrm{Re}[\hat{\varepsilon}(x, y; k)]$.

retrieve a locally homogeneous medium for the random Poisson pattern for $\lambda = 2.09$ μm and 1.26 μm compared to the SHU structure is both qualitative and quantitative. In fact, the spatial non-uniformity of $\mathrm{Re}[\hat{\epsilon}(x, y; k)]$ for the Poisson structure, measured by the standard deviation σ, is consistently greater than that of the SHU structure for the same incoming wavelength. We have included an additional figure that summarizes these findings in Figure S5 of the Supporting Information where we show the consistent difference in spatial non-uniformity for the Poisson patterns, quantified by both σ and $\langle \mathrm{Im}[\hat{\epsilon}(x, y; k)] \rangle$. In Figure S5, we have included the MscalePINN's prediction on the single realization beyond the k_0 critical value in the grey-shaded region, where the relative L_1 error was higher with a value of 14%. We also note that for the SHU array, the real part of $\hat{\epsilon}(x, y; k)$ becomes less homogeneous as we approach the edge of the predicted transparency region. In this case, the MscalePINN continues to accurately retrieve a locally homogeneous effective medium until the predicted edge of $k_{th} \approx 5.4$ μm^{-1}, while it fails for the Poisson array far from this critical value. This scenario supports the conclusion that it is easier to retrieve a locally homogeneous effective medium for SHU structures compared to traditional Poisson random media, and that the SHU local homogenization eventually fails at larger incident wave vectors than their Poisson counterparts. In the next section, we will address the effects of size scaling on the MscalePINN predictions of the $\hat{\epsilon}(x, y; k)$ retrieved permittivity distribution.

3.4. Transparency of Finite-Size SHU Structures

Recent work by Torquato and Kim[16,17] led to an exact non-local strong-contrast expansion of the effective dynamic dielectric tensor $\epsilon(x, y)$ in the thermodynamic limit,[16] and more recently they extended these results beyond the long-wavelength regime for layered and transversely isotropic media.[17] Their work provides an analytical prediction for the wavelength range in which SHU structures achieve perfect transparency or, equivalently, for the wavelength regime where the effective dielectric constant has a zero imaginary part. However, to the best of our knowledge, no previous work has established if this transparency prediction is modified by finite-size arrays. In order to address this open question we performed a study over several SHU arrays with different sizes and numbers of pillars $N = 299$, 633, 1002, and 1553. We also computed the structure factors for the corresponding point patterns and displayed the results in Figure S6 of the Supporting Information. Interestingly, we note that characteristic stealthy hyperuniform behavior begins to manifest itself already at relatively small N.

In **Figure 5** we display the retrieved effective permittivity $\hat{\epsilon}(x, y; k)$ for these four stealthy hyperuniform structures with parameters $\chi = 0.3$, $\epsilon_r = 4.0$, and $\phi = 0.25$, which were kept constant for all the arrays to compare with the theoretical predictions for the infinite bulk limit shown in ref. [17]. We train a 4-scale MscalePINNs with 2 layers and 64 neurons each using FEM computed forward fields at plane wave excitation wavelength $\lambda = 6.28$ μm, corresponding to the regime of perfect transparency predicted by Torquato et al.[17] We display the real part of the retrieved permittivity profiles $\hat{\epsilon}(x, y; k)$ in order of increasing array size in Figure 5a–d, and compute the mean and standard deviation inside of the array region. The average of the retrieved effective dielectric function for the four structures is $\langle \mathrm{Re}[\hat{\epsilon}(x, y; k)] \rangle = 1.7 \pm 5.9\%$ and $\langle \mathrm{Im}[\hat{\epsilon}(x, y; k)] \rangle = 10^{-4}$, independent of the array size. This result is extremely close to the predicted value in ref. [17] for transversely isotropic media with $\chi = 0.3$, $\epsilon_r = 4.0$, and $\phi = 0.25$. Furthermore, due to the relatively large wavelength regime, the predicted $\hat{\epsilon}$ agrees with the Bruggeman mixing formula of $\epsilon_{brugg} = 1.75$ with a 3% error, and the structures reproduced the original fields with a 9% relative L_1 error. Therefore, from this analysis, we conclude that finite-size scaling does not perturb appreciably the value of the retrieved dielectric constant of SHU arrays. In the next sections, we conclude our analysis by first demonstrating that MscalePINN can be employed to retrieve locally homogeneous effective media that leverage the isotropic response featured by SHU structures, a property that is highly desired for engineering angle-insensitive effective media of finite size. Furthermore, we show a relevant application to photonics inverse design, specifically in the context of waveguiding and focusing structures. Lastly, we discuss how it is possible to employ MscalePINN for the inverse design of binary optical metamaterials.

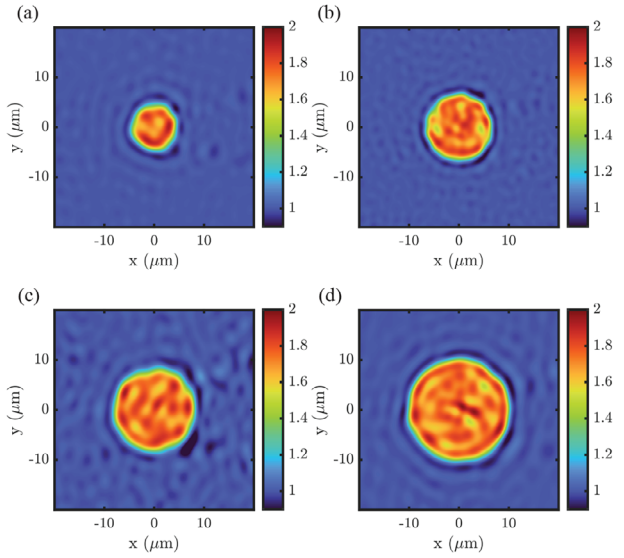

Figure 5. Panels displaying the real part of $\hat{\epsilon}(x, y; k)$. a)-d) Scaling analysis of the retrieved effective medium performed on four SHU arrays with 299, 633, 1002, and 1553 particles, respectively, and $\langle d \rangle / \lambda = 0.06$. The average of MscalePINNs's permittivity profile displayed in the four panels all have a computed average value within the region of $\langle \mathrm{Re}[\hat{\epsilon}(x, y; k)] \rangle = 1.70 \pm 5.9\%$, independently of the size of the hyperuniform array.

3.5. Isotropic Response of Finite-Size SHU Structures

The development of complex photonic media with isotropic scattering responses is important to for engineering device applications as it naturally result in robust performances with enhanced light-matter coupling. In order to demonstrate numerically that locally homogeneous stealthy hyperuniform arrays are isotropic with respect to the direction of the incoming electric field, we perform angle-dependent simulations on a stealthy hyperuniform array $N = 236$ with $\chi = 0.5$, $\epsilon_r = 3.0$, and $\phi = 0.20$. In **Figure 6a**

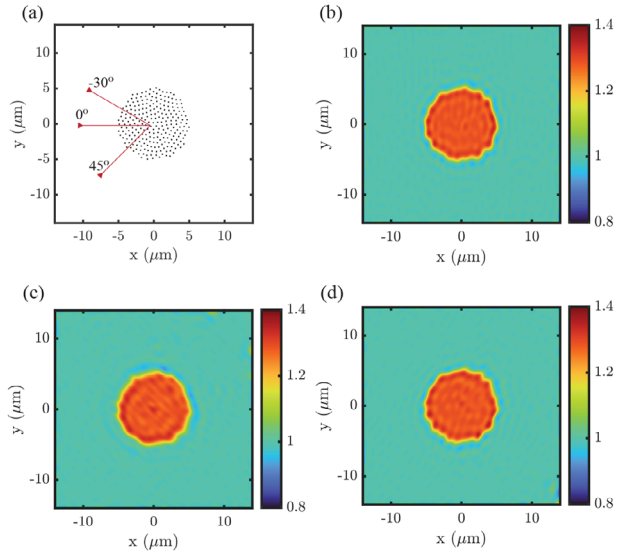

Figure 6. a) Schematics of the angles employed to study the angular independence in the homogenization of a SHU array of $N = 236$ particles, $\chi = 0.5$, $\epsilon_r = 3.0$, $\langle d \rangle / \lambda = 0.09$, and packing fraction $\phi = 0.20$. b–d) MscalePINN's reconstructed real part of $\hat{\epsilon}(x, y; k)$. These locally homogeneous permittivity profiles $\hat{\epsilon}(x, y; k)$ were retrieved by training on incident light with wavelength $\lambda = 6.28$ μm at three different angles: $\theta = 0°, 45°, -30°$. The averages of $\langle \mathrm{Re}[\hat{\epsilon}(x, y; k)] \rangle$ in the homogenized regions agree and show that the homogenization is independent of the angle of incidence.

we display the SHU array with the angles employed to generate the forward FEM numerical simulations utilized to train the 4-scale MscalePINNs with 4 layers by 64 neurons each. As in the previous studies, we have included the corresponding structure factor $S(\boldsymbol{k})$ in the Supporting Information Figure S7, together with the inverse training FEM fields displayed in Figure S8. The retrieved locally homogeneous permittivity profiles $\hat{\epsilon}(x, y; k)$ are shown in Figure 6b–d, displaying the MscalePINNs precision in capturing contour features on the boundary of the hyperuniform array. All three permittivity profiles present an accurate agreement in the real and imaginary part of $\hat{\epsilon}(x, y; k)$, with $\langle \mathrm{Re}[\hat{\epsilon}(x, y; k)] \rangle = 1.28 \pm 3\%$ and $\langle \mathrm{Im}[\hat{\epsilon}(x, y; k)] \rangle = 10^{-4}$, while the relative L_1 error was close to 5% against the original field in all three cases. To confirm that the three locally homogeneous effective media have indeed the same electromagnetic response, we selected the permittivity profile trained with the incoming radiation at $\theta = 0°$ and performed two forward FEM simulations at $\theta = 45°$ and $-30°$. We then computed the relative L_1 error between the forward field used in training on the SHU array at $\theta = 45°$ and $-30°$ and the one just recomputed by utilizing the homogenized structure trained with the incoming radiation at $\theta = 0°$. Both errors were close to 10%, showing that the effective medium retrieved by MscalePINNs when trained with incoming radiation at $\theta = 0°$ reproduced the same training FEM field when the incoming angle was set to $\theta = 45°$ and $-30°$. Furthermore, we show that the retrieved contour displayed in the three structures from Figure 6 is important to reproduce the original field distribution with high fidelity. When we considered a structure with perfectly circular $\epsilon(x, y; k)$ with radius $L/2$ and a constant Bruggeman value, we obtained a field with a L_1 relative error of ∼26% over the original training field. This shows that MscalePINN's $\hat{\epsilon}(x, y; k)$ accurately detects even the very small features that are present in the contour of the array in Figure 6a. In conclusion, we showed numerically that single-realization finite-size SHU arrays feature an isotropic homogenized response to the incoming radiation and we present evidence that MscalePINN can be employed to retrieve topological features without a priori knowledge of the object boundary with high accuracy.

3.6. MscalePINN for the Design of a SHU Waveguide

There has been growing interest in exploiting the transparency region of SHU structures due to their robustness against multiple scattering. In fact, recent work has shown that this transparency regime can be leveraged to improve the design of photonic materials and devices such as waveguides.[21–23] Here, we employ MscalePINN to demonstrate the retrieval of a locally homogeneous medium corresponding to a stealthy hyperuniform photonic array in a rectangular waveguide geometry similar to the one originally investigated in ref. [22] to demonstrate enhanced wave transport beyond the diffusive regime. Specifically, we consider the rectangular stealthy hyperuniform distribution of $N \approx 700$ cylindrical scatterers with $\epsilon_r = 2.2$ inside a waveguide with stealthiness $\chi = 30\%$ shown in **Figure 7a**. This stealthiness value is within the range discussed by Cheron et al. We then performed a forward FEM simulation and trained the MscalePINN on the inverse training dataset field shown in Figure 7c with $k_0 = 1.57$ μm^{-1}, which is away from the predicted transparency threshold wavenumber $k_{th} \approx 3.0$ μm^{-1}. The retrieved effective medium $\mathrm{Re}[\hat{\epsilon}(x, y; k)]$ is shown in panel (b), and its distribution of values is displayed in the histogram in panel (e). We found that the average value for the real part of the

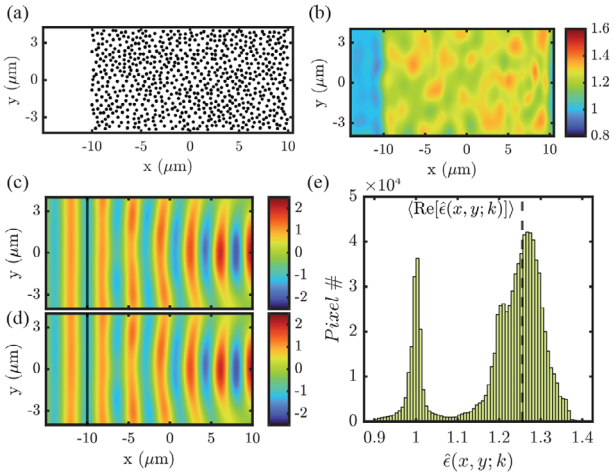

Figure 7. a) Geometry employed for the forward FEM field simulation displayed in panel (c) with $k_0 = 1.57$ μm^{-1}, where the blank space on the left is intended for wave propagation outside of the structure. b) Inversely retrieved $\mathrm{Re}[\hat{\epsilon}(x, y; k)]$ with its distribution displayed in panel (e), where we have labeled the average value $\langle \mathrm{Re}[\hat{\epsilon}(x, y; k)] \rangle = 1.252$ inside the effective medium. The distribution of values is bimodal around the effective medium average and air outside of the structure. d) The real part of the forward FEM field computed through the inversely retrieved structure shown in panel (b).

permittivity was $\langle \mathrm{Re}[\hat{\varepsilon}(x, y; k)] \rangle = 1.252 \pm 6\%$. In addition, the L^2 cumulative training error was lower than 10^{-4}, while the relative L_1 error computed on the homogeneous $\hat{\varepsilon}(x, y; k)$, displayed in panel (d), and the original field was 3%. These results show that MscalePINN can be employed to accurately retrieve a locally homogeneous effective medium in a waveguide configuration, leveraging the enhanced transparency properties of SHU arrays of scattering nanocylinders. This enables the efficient design of materials and devices with desired permittivity distributions and enhanced optical transparency beyond the diffusion limit of traditional random media, a problem of great relevance for photonics applications.[22] This includes the ability to design spatially inhomogeneous and compact metamaterials that implement low-loss mode transformation and control of the effective index of refraction for on-chip integrated photonic couplers in the near-infrared spectral range.[9] In the next and final section, we describe an implementation of the MscalePINN architecture that enables the inverse design of optical materials with a choice of binary permittivity values.

3.7. MscalePINN for the Inverse Design of Binary Optical Materials

Throughout this paper, we have shown that MscalePINN is a powerful extension of traditional single-scale PINN in the context of photonic inverse design from the long- to short-wavelength regime. In particular, using k_{th} as a metric, we displayed the MscalePINN's ability to retrieve effective media for wavelengths close to the multiple scattering regime. However, the retrieved structures so far allowed for a continuously varying permittivity, a feature that makes their fabrication very challenging. In order to overcome this limitation, we introduce here a different MscalePINN architecture that enables the accurate inverse design of binary optical materials and metamaterials with an optimal permittivity distribution $\hat{\varepsilon}(x, y; k)$ to achieve a functionality. Importantly, in this implementation the binary values of the retrieved permittivity profile can be largely determined by the designer, thus making our approach compatible with a large class of available optical materials.

So far, we have employed the multiscale architecture displayed in Figure 1, where the final layer's output $\hat{u}$ is a linear combination of the sub-networks' outputs u_i. As a result, the effective medium featured a continuous distribution of $\hat{\varepsilon}(x, y; k)$ values, only limited by the PDE and synthetic data characteristics. However, in most engineering applications the effective medium design is constrained by the limitations of available materials, i.e., we must choose a well-characterized material with a suitable refractive index. When considering the inverse design of the optimal shape of a functional optical structure in air, given the availability of a chosen optical material, we must modify the MscalePINN to enable retrieving a spatial distribution $\hat{\varepsilon}(x, y; k)$ with binary values corresponding to the one of air and of the chosen material. We achieve this task by bounding the network's final output with a custom sigmoid activation function:

$$\sigma_{cust} = \frac{\gamma}{1 + e^{-\xi * x}} + \eta \tag{27}$$

where γ, ξ, η are user-defined parameters determining the material and background effective permittivity of the retrieved effective medium. In particular, η is the background medium, usually set to 1.0 (air), while γ determines the epsilon values above 1.0. For example, an effective medium of relative permittivity 2.2 immersed in air should have $\gamma = 1.2$ and $\eta = 1.0$. Finally, ξ is the slope of the final layer's sigmoid function, determining how sharp the binarization in $\hat{\varepsilon}$ should be during training. This is the hardest parameter to set, as higher values of ξ do ensure sharper transitions, but MscalePINN becomes difficult to train due to very large gradients during the back-propagation of the network. These large gradients are caused by the large derivatives of the sigmoid function that approximates a sharp step function. In practice, we experienced that it is safer to keep ξ at the default value of 1.0 during training, and in the examples that follow, we will describe an alternative way to improve binarization while keeping the training stable. Furthermore, in the following discussion, we will consider two different scenarios, namely the retrieval of a constant-epsilon medium (the homogenization case) and a binary-epsilon medium embedded in an air background (the multiple-scattering case). We refer to the latter case as the multiple-scattering one because we consider plane wave excitations close to the given structure's k_{th} value. The MscalePINN architectures employed hereafter are similar, as they both use a multiscale network such as the one displayed in Figure 1 for the real and imaginary part of the electric field. Still, they differ in the coupled $\hat{\varepsilon}$ network that retrieves the permittivity profile. For the homogenization architecture, we employ a full-domain single-scale network with a binary sigmoid output. Instead, we employ a multiscale network with a binary output trained only in a square region of interest for the multiple-scattering case. In practice, what this means is that in the homogenization case, we let MscalePINN choose where the transition between air and the material occurs in the computational domain Ω, while in the multiple-scattering case, we let MscalePINN determine the transition between the two materials only within a region of interest while keeping $\hat{\varepsilon}$ constant at unit values outside.

In **Figure 8a** we display an example of MscalePINN binarization for a square SHU structure under plane wave excitation at $\lambda = 3.0$ μm. For this example, we have picked the same structural parameters from the arrays in Figure 2, but we cut the array in a square instead of a circle to display the versatility of MscalePINN when retrieving objects with sharp corners. In Figure 8b, we have overlayed the SHU array to the field retrieved with a forward FEM simulation on the homogeneous structure. In this simulation, we chose to find an effective medium with $\hat{\varepsilon} = 1.8$, so we set $\gamma = 0.8$, $\xi = 1.0$, $\eta = 1.0$. As the results show, the effective medium is binarized, with a relative L_1 error on the true field of 6%. In Figure 8c we display the binary effective medium retrieved when the square SHU structure employed in panel (b) is excited by a plane wave at $\lambda = 2.0$ μm. For this wavelength, it is impossible to retrieve a single homogeneous medium because we are at the edge of the transparency region, with $k_0 = 3.14$ and $k_{th} = 3.5$, so we restrict the training of the $\hat{\varepsilon}$ MscalePINN to a square subset (x_{sq}, y_{sq}) of Ω in the central region with dimensions 11 μm × 11 μm. To display the power of MscalePINN, we set $\gamma = 0.5$, $\xi = 1.0$, $\eta = 1.5$, which are meant to model a binary material with

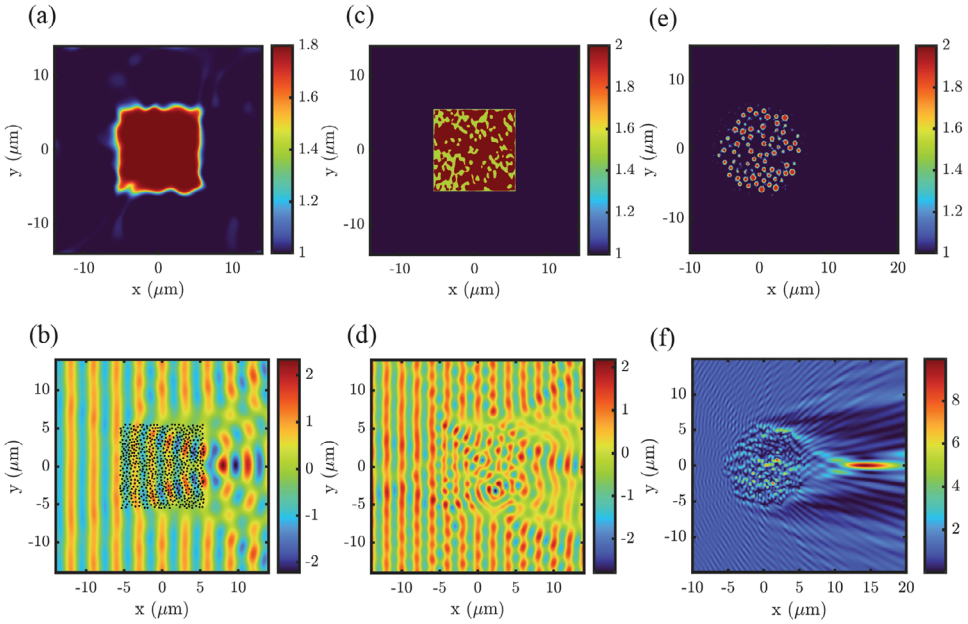

Figure 8. a) Real part of the binary structure retrieved on the $\lambda = 3$ μm field using the modified MscalePINN approach with the custom sigmoid activation function from Equation 27. b) Real part of the field from the forward simulation on the structure displayed in (a) with the original SHU pattern superimposed. The error between the forward field in b) and the original was 6%. c) Real part of the two-level binarized structure retrieved at $\lambda = 2.0$ μm, or $k_0 = 3.14$ μm^{-1}, on the SHU pattern shown in panel (b). d) The real part of the forward field scattered through the binarized structure displayed in panel (c), which had a relative L_1 error of 12% on the original. e) Real part of the focusing effective medium retrieved by MscalePINN at $\lambda = 1.0$ μm with $\hat{\varepsilon} = 1.9$. f) For better visualization, we display the focusing intensity of the total field obtained by performing a forward FEM simulation through the effective medium displayed in panel (e).

$\hat{\varepsilon}_1 = 1.5$ and $\hat{\varepsilon}_2 = 2.0$. To ensure a proper binarization, we add the additional loss term $\mathcal{L}_{bin}$ to Equation 23. This new term is defined as:

$$\mathcal{L}_{bin}(\tilde{\theta}; \mathcal{N}_{bin}) = \frac{1}{|\mathcal{N}_{bin}|} \sum_{(x_{sq}, y_{sq}) \in \mathcal{N}_{bin}} \left|\left| \Theta(\hat{\varepsilon}(x_{sq}, y_{sq}; k)) - \hat{\varepsilon}(x_{sq}, y_{sq}; k) \right|\right|_2^2 \quad (28)$$

here, Θ is a step function centered at $\eta + \gamma/2$. We switch on $\mathcal{L}_{bin}$ after 1/4 of the total training epochs to ensure that the $\hat{\varepsilon}$ MscalePINN retrieves is more binarized. In panel (c) we display the binarized structure obtained on post-processing the final output of MscalePINN with the Θ function described above. The pre-processed output is displayed in section S9 of the Supporting Information. This is a common strategy employed in optimization algorithms that are constrained by fabrication requirements, and it ensures that the final output of MscalePINN is very close to a fabricable structure.[70] The L^2 cumulative training error of MscalePINN to produce the pre-processed structure is 10^{-3}, while the relative L_1 error on both the pre-processed and binarized structure shown in panel (d) is 13%. Finally, we inversely retrieve the structure of a binary material from training on the focusing fields studied in ref. [71], with $\lambda = 1.0$ μm. The training datasets corresponding to the focusing field are shown in section S10 of the Supporting Information. Panel (f) displays the intensity of the total field obtained with a forward simulation on the structure retrieved in panel (e), demonstrating a clear focusing behavior at a distance of 15 μm. For this simulation, we chose $\gamma = 0.9$, $\xi = 1.0$, $\eta = 1.0$, corresponding to pillars with $\hat{\varepsilon} = 1.9$. Despite the wavelength being in the multiple-scattering regime, the retrieved structure accurately reproduced the focusing field with an L_1 relative error below 14%.

4. Conclusions

In this article, we developed and applied the MscalePINN framework to inversely retrieve the effective dielectric permittivity of finite-size arrays of scattering nanocylinders with stealthy hyperuniform and uncorrelated Poisson geometries. Through numerous examples, we established that MscalePINN is a necessary powerful extension of traditional single-scale PINN architectures when dealing with multiple scattering contributions in the retrieval of the effective medium parameters of complex media, thus enabling a systematic methodology to retrieve the general spatial dependence of the effective dielectric behavior of scattering arrays in device-relevant geometries beyond traditional homogenization theories. In particular, we demonstrated the existence of a transparency region in finite-size SHU structures beyond the long-wavelength approximation, enabling the retrieval of effective and isotropic locally homogeneous media even without disorder-averaging, in contrast to the case of uncorrelated Poisson random patterns. Specifically, we found that the retrieved permittivity distribution $\hat{\varepsilon}(x, y; k)$ obtained for a single-realization of stealthy hyperuniform disorder agrees with the ensemble average calculations with an error close to 1%, whereas a large standard deviation of $\hat{\varepsilon}(x, y; k)$ is obtained for Poisson arrays of comparable sizes. Importantly, we showed that locally homogeneous SHU structures feature isotropic responses to an incoming plane

wave excitation that are not appreciably modified by their finite size, which is a highly desired characteristic for the engineering of angle-insensitive photonic media and metamaterial devices. Furthermore, we applied our approach to accurately retrieve a locally homogeneous medium in a rectangular waveguide geometry corresponding to a scattering SHU array with enhanced transparency. Lastly, we show how to achieve the inverse design of binary optical media trained on desired field profiles and material parameters using a modified MscalePINN architecture that generates structures suitable for experimental demonstration using available nanofabrication techniques. These results enable the efficient design of functional photonic structures that operate in the multiple scattering regime and motivate future developments of MscalePINN for accurate inverse shape (topological) identification and remote sensing applications at optical wavelengths. In conclusion, our work provides an efficient route towards the discovery of novel structures with effective medium properties arising from the interaction of disordered scattering geometries and vector or scalar waves of arbitrary nature, including acoustic, mechanical, and quantum wave phenomena.

Supporting Information

Supporting Information is available from the Wiley Online Library or from the author.

Acknowledgements

L.D.N. acknowledges the support from the U.S. Army Research Office, RF-Center managed by Dr. T. Oder (Grant #W911NF-22-2-0158). S.T. acknowledges the support of the U.S. Army Research Office under Cooperative Agreement No. W911NF-22-2-0103. The work of W.C. is supported by the US National Science Foundation grant DMS-2207449.

Conflict of Interest

The authors declare no conflicts of interest.

Data Availability Statement

The data and models that support the findings of this study are available upon reasonable requests.

Keywords

inverse design, multiscale, neural networks, optical materials, photonics

Received: December 2, 2024
Revised: April 23, 2025
Published online: May 19, 2025

[1] S. Torquato, F. H. Stillinger, *Phys. Rev. E* **2003**, *68*, 041113.
[2] S. Torquato, *Phys. Rep.* **2018**, *745*, 1.
[3] S. Torquato, G. Zhang, F. Stillinger, *Phys. Rev. X* **2015**, *5*, 021020.
[4] M. A. Klatt, P. J. Steinhardt, S. Torquato, *Proceedings of the National Academy of Sciences* **2022**, *119*, e2213633119.
[5] Z. Ma, S. Torquato, *J. Appl. Phys.* **2017**, *121*, 244904.
[6] F. Sgrignuoli, S. Torquato, L. D. Negro, *Phys. Rev. B* **2022**, *105*, 064204.
[7] F. M. Izrailev, A. A. Krokhin, N. M. Makarov, *Phys. Rep.* **2012**, *512*, 125.
[8] D. Chen, S. Torquato, *Acta Mater.* **2018**, *142*, 152.
[9] P. Cheben, R. Halir, J. H. Schmid, H. A. Atwater, D. R. Smith, *Nature* **2018**, *560*, 565.
[10] G. Gkantzounis, T. Amoah, M. Florescu, *Phys. Rev. B* **2017**, *95*, 094120.
[11] W. Man, M. Florescu, E. P. Williamson, Y. He, S. R. Hashemizad, B. Y. C. Leung, D. R. Liner, S. Torquato, P. M. Chaikin, P. J. Steinhardt, *Proceedings of the National Academy of Sciences* **2013**, *110*, 15886.
[12] R. Degl'Innocenti, Y. D. Shah, L. Masini, A. Ronzani, A. Pitanti, Y. Ren, D. S. Jessop, A. Tredicucci, H. E. Beere, D. A. Ritchie, *Sci. Rep.* **2016**, *6*, 19325.
[13] H. Zhang, H. Chu, H. Giddens, W. Wu, Y. Hao, *Appl. Phys. Lett.* **2019**, *114*, 053507.
[14] S. Gorsky, W. A. Britton, Y. Chen, J. Montaner, A. Lenef, M. Raukas, L. D. Negro, *APL Photonics* **2019**, *4*, 110801.
[15] M.-J. Sun, X.-Y. Zhao, L.-J. Li, *Opt. Lett.* **2018**, *43*, 4049.
[16] S. Torquato, J. Kim, *Phys. Rev. X* **2021**, *11*, 021002.
[17] J. Kim, S. Torquato, *Opt. Mater. Express* **2024**, *14*, 194.
[18] L. Alhaïtz, J.-M. Conoir, T. Valier-Brasier, *Phys. Rev. E* **2023**, *108*, 065001.
[19] G. J. Aubry, L. S. Froufe-Pérez, U. Kuhl, O. Legrand, F. Scheffold, F. Mortessagne, *Phys. Rev. Lett.* **2020**, *125*, 127402.
[20] K. Vynck, M. Burresi, F. Riboli, D. S. Wiersma, *Nat. Mater.* **2012**, *11*, 1017.
[21] M. M. Milošević, W. Man, G. Nahal, P. J. Steinhardt, S. Torquato, P. M. Chaikin, T. Amoah, B. Yu, R. A. Mullen, M. Florescu, *Sci. Rep.* **2019**, *9*, 20338.
[22] E. Cheron, S. Felix, J.-P. Groby, V. Pagneux, V. Romero-Garcia, *Appl. Phys. Lett.* **2022**, *121*, 061702.
[23] V. Romero-García, E. Cheron, S. Kuznetsova, J. Groby, S. Felix, V. Pagneux, L. M. Garcia-Raffi, *APL Materials* **2021**, *9*, 101101.
[24] J. Kim, S. Torquato, *Proceedings of the National Academy of Sciences* **2020**, *117*, 8764.
[25] G. Gkantzounis, M. Florescu, *Crystals* **2017**, *7*, 353.
[26] H. Zhang, W. Wu, Q. Cheng, Q. Chen, Y.-H. Yu, D.-G. Fang, *IEEE Trans. Antennas Propag.* **2022**, *70*, 7513.
[27] M. Florescu, S. Torquato, P. J. Steinhardt, *Proc. Natl. Acad. Sci.* **2009**, *106*, 20658.
[28] W. Shi, D. Keeney, D. Chen, Y. Jiao, S. Torquato, *Phys. Rev. E* **2023**, *108*, 045306.
[29] L. Tsang, J. A. Kong, K.-H. Ding, *Scattering of electromagnetic waves. Theories and applications*, Wiley series in remote sensing. Wiley, New York, **2000**.
[30] L. Dal Negro, *Waves in complex media: fundamentals and device applications*, Cambridge University Press, New York, **2022**.
[31] A. Ishimaru, *Wave propagation and scattering in random media*, Academic Press, New York, **1978**.
[32] Z. Wei, X. Chen, *IEEE Trans. Geosci. Remote Sens.* **2019**, *57*, 1849.
[33] P. Mehta, M. Bukov, C.-H. Wang, A. G. R. Day, C. Richardson, C. K. Fisher, D. J. Schwab, *Phys. Rep.* **2019**, *810*, 1.
[34] J. Jiang, M. Chen, J. A. Fan, *Nat. Rev. Mater.* **2021**, *6*, 679.
[35] J. Schmidt, M. R. G. Marques, S. Botti, M. A. L. Marques, *npj Comput. Mater.* **2019**, *5*, 1.
[36] Y. Sun, Z. Xia, U. S. Kamilov, *Opt. Express* **2018**, *26*, 14678.
[37] B. Xiong, Y. Xu, W. Li, W. Ma, T. Chu, Y. Liu, *Adv. Opt. Mater.* **2024**, *12*, 2302200.
[38] W. Ma, Y. Xu, B. Xiong, L. Deng, R.-W. Peng, M. Wang, Y. Liu, *Adv. Mater.* **2022**, *34*, 2110022.
[39] D. Zhu, Z. Liu, L. Raju, A. S. Kim, W. Cai, *ACS Nano* **2021**, *15*, 2318.

[40] Z. A. Kudyshev, A. V. Kildishev, V. M. Shalaev, A. Boltasseva, *Appl. Phys. Rev.* **2020**, *7*, 021407.
[41] P. R. Wiecha, O. L. Muskens, *Nano Lett.* **2020**, *20*, 329.
[42] I. Malkiel, M. Mrejen, A. Nagler, U. Arieli, L. Wolf, H. Suchowski, *Light: Sci. Appl.* **2018**, *7*, 60.
[43] W. Ma, F. Cheng, Y. Liu, *ACS Nano* **2018**, *12*, 6326.
[44] Y. Xu, B. Xiong, W. Ma, Y. Liu, *Prog. Quantum Electron.* **2023**, *89*, 100469.
[45] W. Ma, Z. Liu, Z. A. Kudyshev, A. Boltasseva, W. Cai, Y. Liu, *Nat. Photonics* **2021**, *15*, 77.
[46] J. R. Capers, L. D. Stanfield, J. R. Sambles, S. J. Boyes, A. W. Powell, A. P. Hibbins, S. A. R. Horsley, *Phys. Rev. Appl.* **2024**, *21*, 014005.
[47] J. R. Capers, S. J. Boyes, A. P. Hibbins, S. A. R. Horsley, *Commun. Phys.* **2021**, *4*, 1.
[48] J. R. Capers, S. J. Boyes, A. P. Hibbins, S. A. R. Horsley, *New J. Phys.* **2022**, *24*, 113035.
[49] Z.-Q. J. Xu, L. Zhang, W. Cai, On understanding and overcoming spectral biases of deep neural network learning methods for solving PDEs, **2025**, http://arxiv.org/abs/2501.09987, ArXiv:2501.09987 [math].
[50] S. Wang, H. Wang, P. Perdikaris, *Comput. Meth. Appl. Mech. Eng.* **2021**, *384*, 113938.
[51] Z. You, Z. Xu, W. Cai, MscaleFNO: Multi-scale Fourier Neural Operator Learning for Oscillatory Function Spaces, **2024**, http://arxiv.org/abs/2412.20183, ArXiv:2412.20183 [math].
[52] L. Lu, X. Meng, Z. Mao, G. E. Karniadakis, *SIAM Rev.* **2021**, *63*, 208.
[53] L. Lu, R. Pestourie, W. Yao, Z. Wang, F. Verdugo, S. G. Johnson, *SIAM J. Sci. Comput.* **2021**, *43*, 6, B1105.
[54] M. Raissi, P. Perdikaris, G. E. Karniadakis, *J. Comput. Phys.* **2019**, *378*, 686.
[55] Y. Chen, L. Lu, G. E. Karniadakis, L. Dal Negro, *Opt. Express* **2020**, *28*, 11618.
[56] G. Pang, L. Lu, G. E. Karniadakis, *SIAM J. Sci. Comput.* **2019**, *41*, A2603.
[57] Y. Chen, L. Dal Negro, *APL Photonics* **2022**, *7*, 010802.
[58] R. Riganti, L. Dal Negro, *Appl. Phys. Lett.* **2023**, *123*, 171104.
[59] Y. Sanghvi, Y. Kalepu, U. K. Khankhoje, *IEEE Trans. Comput. Imaging* **2020**, *6*, 46.
[60] Z.-Q. J. Xu, *Commun. Comput. Phys.* **2020**, *28*, 1746.
[61] N. Rahaman, A. Baratin, D. Arpit, F. Draxler, M. Lin, F. Hamprecht, Y. Bengio, A. Courville, in *Proceedings of the 36th International Conference on Machine Learning*. PMLR, **2019** pp. 5301–5310, https://proceedings.mlr.press/v97/rahaman19a.html, ISSN: 2640-3498.
[62] J. C. Wong, C. Ooi, A. Gupta, Y.-S. Ong, *IEEE Trans. Artif. Intel.* **2022**, 1.
[63] B. Ronen, D. Jacobs, Y. Kasten, S. Kritchman, in *Advances in Neural Information Processing Systems*, Vol. *32*. Curran Associates, Inc., **2019**, https://proceedings.neurips.cc/paper/2019/hash/5ac8bb8a7d745102a978c5f8ccdb61b8-Abstract.html.
[64] Z. Liu, W. Cai, Z.-Q. J. Xu, *Commun. Comput. Phys.* **2020**, *28*, 1970.
[65] L. Zhang, W. C. Null, Z.-Q. J. Xu, *Commun. Comput. Phys.* **2023**, *33*, 1509.
[66] A. H. Sihvola, *Electromagnetic mixing formulas and applications*, Number 47 in IEE electromagnetic waves series. Institution of Electrical Engineers, London, **2008**.
[67] M. I. Mishchenko, L. D. Travis, A. A. Lacis, *Multiple scattering of light by particles: radiative transfer and coherent backscattering*, Cambridge University Press, Cambridge, United Kingdom, first paperback edition edition, **2017**.
[68] COMSOL AB, COMSOL Multiphysics v. 6.0, Stockholm, Sweden, **2024**, https://www.comsol.com.
[69] M. Abadi, A. Agarwal, P. Barham, E. Brevdo, Z. Chen, C. Citro, G. S. Corrado, A. Davis, J. Dean, M. Devin, S. Ghemawat, I. Goodfellow, A. Harp, G. Irving, M. Isard, Y. Jia, R. Jozefowicz, L. Kaiser, M. Kudlur, J. Levenberg, D. Mané, R. Monga, S. Moore, D. Murray, C. Olah, M. Schuster, J. Shlens, B. Steiner, I. Sutskever, K. Talwar, et al., TensorFlow: Large-scale machine learning on heterogeneous systems, **2015**, https://www.tensorflow.org/, Software available from tensorflow.org.
[70] R. E. Christiansen, O. Sigmund, *JOSA B* **2021**, *38*, 496.
[71] Y. Zhu, Y. Chen, S. Gorsky, T. Shubitidze, L. Dal Negro, *JOSA B* **2023**, *40*, 1857.